


Research Article

RuCo@P Core-Shell Nanoparticles Filled with Carbon Nanotubes for Highly Effective Catalytic Hydrolysis of Ammonia Borane

Chengfeng Xu,^{1,2} Lan Yang,^{1,2} Zien Liu,^{1,2} and Ye Tao ^{1,2}

¹Hubei Key Laboratory of Advanced Technology for Automotive Components & Hubei Collaborative Innovation Center for Automotive Components Technology (Wuhan University of Technology), Wuhan 430070, China

²Hubei Research Center for New Energy & Intelligent Connected Vehicle, Wuhan University of Technology, Wuhan 430070, China

Correspondence should be addressed to Ye Tao; tao-ye@whut.edu.cn

Received 25 August 2023; Revised 7 December 2023; Accepted 20 December 2023; Published 16 January 2024

Academic Editor: Prakash Bhuyar

Copyright © 2024 Chengfeng Xu et al. This is an open access article distributed under the Creative Commons Attribution License, which permits unrestricted use, distribution, and reproduction in any medium, provided the original work is properly cited.

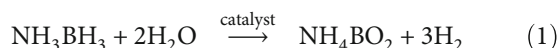
The doping of nonmetals in multiphase metal catalysts can effectively improve the catalytic performance and reduce the catalyst cost. In this study, we synthesized transition metal phosphide (RuCo@P/CNT) catalysts loaded on carbon nanotubes (CNT) using sodium borohydride (NaBH₄) as the reducing agent. The microstructure and phase composition of RuCo@P/CNT nanoparticles were investigated using X-ray photoelectron spectroscopy (XPS), X-ray diffraction (XRD), transmission electron microscopy (TEM), and BET. RuCo@P/CNT nanoparticles show superior catalytic activity and cycle stability in the catalytic ammonia borane hydrolysis process compared to Ru/CNT and RuCo/CNT nanoparticles, retaining 65.74% of their initial catalytic activity after 5 reaction cycles. The test yielded values for turnover frequency and activation energy of 327.33 min⁻¹ and 36.77 kJ·mol⁻¹, respectively. Additionally, a kinetic isotope effect value of 2.61 for H₂O/D₂O showed that O-H bond breaking in proportional acceptor water is the decisive step in the dehydrogenation of ammonia borane, and based on this discovery, a specific mechanism for the catalytic hydrolysis of AB by RuCo@P NPs is postulated.

1. Introduction

In recent years, with the rapid growth of population and the rapid improvement of industrial level, fossil energy has been rapidly consumed, and the utilization of hydrogen energy has gradually become a focus of attention [1]. Among the green energies, hydrogen energy is considered one of the most important candidates due to its higher density (120 MJ/kg), rich reserves, low density (0.0899 g/L), zero emission, and broad application fields. The H₂ production, storage, and hydrogen regeneration are the main steps of the hydrogen production [2]. However, hydrogen safety is poor, and under physical hydrogen storage conditions, hydrogen embrittlement may occur with metals, leading to a decrease in the strength of storage tanks. These factors all pose challenges to the storage of hydrogen as well as transportation. In chemical hydrogen storage, hydrogen elements exist in the form of ions or atoms, such as ammonia borane

[3] and sodium borohydride [4], greatly improving adsorption stability and hydrogen safety, thus receiving widespread attention [5]. Due to the existence of chemical bond such as ionic bonds, the interaction between hydrogen and other elements in chemical hydrogen storage is stronger than that in physical hydrogen storage, and hydrogen can rapidly evolve under certain conditions [6]. As an emerging material for hydrogen storage with high potential, ammonia borane (NH₃BH₃, AB) has a theoretical hydrogen storage capacity reaching 19.6 wt% and 146 g·L⁻¹. The aqueous solution of AB is nontoxic and harmless under environmental conditions and has high stability [7]. Equation (1) demonstrates that AB can hydrolyze to yield 3 moles of hydrogen per mole with the suitable catalyst. Its high portability in hydrogen storage applications is attracting more and more attention [8, 9]. Creating reliable and affordable catalysts is essential for the hydrolysis of AB to produce hydrogen. Among them, various types of metal catalysts have been studied the most

[10], and noble metals such as Pd [11], Pt [12], and Ru [13] exhibit excellent catalytic performance. In addition, due to the synergistic effect between multiple metals that can enhance catalytic activity, not only noble and non-noble metal NPs but also their composite materials have been subjected to hydrolysis dehydrogenation testing. Ru-based NPs, including bimetallic RuCo, RuCu [14], and RuNi [15] alloys, exhibit extremely high activity for the hydrolysis and dehydrogenation of AB.



Transition metal phosphides (TMPs) are highly regarded for their excellent activity and long-term durability. Its particular structure gives it properties similar to those of precious metals and is known as a “quasi-platinum catalyst” with a wide range of catalytic applications, having been extensively applied in hydrodesulfurization and hydrogen evolution reactions [16–18]. Recently, numerous studies have investigated the effective TMPs in the catalytic dehydrogenation of AB. Yang et al. [19] synthesized a Ni-Fe-P/Ni ternary catalyst using a one-step chemical plating method, which exhibited better catalytic activity compared to the Ni-Fe/Ni catalyst. Wang et al. [20] reported that the noble metal-free Co@Co₂P/N with CNT as a carrier has better catalytic performance than the Co@Co₂/N catalyst formed by undoped nonmetallic P. Qu et al. [21] obtained good outcomes getting NiCoP/OPC-300 loaded into oxygen-doped porous carbon transformed with ZIF-67. Although transition metal phosphides are easy to obtain and have good catalytic efficiency, precious metals still have unparalleled advantages in the field of catalytic AB hydrogen evolution. The incorporation of precious metals as cocatalysts stands out as a potent strategy for significantly enhancing the activity of heterogeneous catalysts. Asim et al. [22] reported catalysts Au/Ni₂P and Au/CoP with high synergistic effects between gold nanoparticles and metal phosphides. Compared with the original Ni₂P and CoP, the activity increased by 4.8 and 1.7 times, respectively. Qu et al. [11] synthesized transition metal phosphide nanoparticles (Pd@Co@P) supported by reduced graphene oxide using a one-step in situ synthesis method. It was found that the synergistic electronic interaction between metal phosphides can effectively improve catalytic performance. Wan et al. [23] achieved a visual-driven strategy of generating H₂ through AB hydrolysis using NiPt nanoparticles supported by phosphorus-doped titanium dioxide (NiPt/P-TiO₂) as photocatalysts. Ru is recognized as one of the best metal catalysts for the hydrolysis of AB [24]; however, there are few researches on Ru-based phosphides for this reaction. This scarcity serves as inspiration for our investigation into Ru-based transition metal phosphide catalysts.

Dispersion of metal nanoparticles (NPs) is a crucial factor in the activity of catalysts. Therefore, surface modification of catalyst systems using porous matrices can control the stability of dispersions and improve catalytic activity by increasing the number of active sites [25]. Carbon nanotubes (CNT) are widely used in catalysis because of their excellent

electron conduction properties, large specific surface area, and good stability, making them ideal catalyst carriers. The application of CNT in loaded Ni, Co-based alloy catalysts has been reported extensively recently [26]. Wang et al. [20] embedded uniformly dispersed Co@Co₂P nanoparticles into N-doped carbon nanotube polyhedral, which exhibited excellent catalytic performance. Liu et al. [27] synthesized a nitrogen-fixing carbon nanotube that encapsulates Fe and Co nanoparticles under a nitrogen atmosphere. Chen et al. [28] loaded the Pt-Ru nanoparticles on carbon nanotubes and explored the synergistic effect of bimetallic catalysts.

In this research, we used a one-pot coreduction technique to synthesize RuCo@P/CNT. Synthetic product Ru₁Co₁₀@P₅/CNT catalyzes AB hydrolysis to produce hydrogen at 25°C with a turnover frequency value (TOF) value of 327.33 min⁻¹, which is twice of the Ru₁Co₁₀/CNT catalyst (159.61 min⁻¹), and its reaction activation energy (*E_a*) is 36.77 kJ·mol⁻¹. Thus, Ru₁Co₁₀@P₅/CNT has high catalytic activity and good kinetic performance.

2. Experimentation

2.1. Chemical Substances. There was no purification of any chemicals; they were all commercially available. The reaction solvent is deionized water. The following are the chemical substances used: ruthenium trichloride (RuCl₃, Merck Reagent, 98%), cobalt chloride hexahydrate (CoCl₂·6H₂O, Merck Reagent, 98%), ammonia borane (NH₃BH₃, Merck Reagent, 98%), sodium hypophosphite (NaH₂PO₂, Merck Reagent, 99%), anhydrous ethanol (C₂H₅OH, Sinopharm Reagent, 99.8%), sodium borohydride (NaBH₄, Sinopharm Reagent, 96%), and carbon nanotubes (CNT, Merck Reagent, 98%).

2.2. Synthesis of RuCo@P/CNT Catalysts. Initially, a 25 mL double-necked flask was utilized to disperse 10 mg of carbon nanotubes (CNT) into 5 mL of deionized water through a five-minute sonication process, ensuring uniform dispersion. Subsequently, a mixture was prepared by adding 1.25 mL of a cobalt chloride solution (CoCl₂, 0.04 mol·L⁻¹), 1 mL of a sodium hypophosphite solution (NaH₂PO₂, 0.05 mol·L⁻¹), and 1 mL of a ruthenium chloride solution (RuCl₃, 0.005 mol·L⁻¹) to the flask. The mixture was then vigorously stirred at a rate of 500 r/min.

To introduce the reducing agent NaBH₄ (1 mol·L⁻¹), a continuous pressure-falling funnel was connected to one neck of the flask. The other neck was attached to a gas tube, which was employed to collect the gas generated during the reaction. Throughout the reduction process, the magnetic stirrer was consistently operated at 500 rpm, while the temperature of the water bath was maintained at 25°C.

Subsequently, the RuCo@P/CNT catalyst was synthesized through a series of steps involving centrifugation and multiple washes using anhydrous ethanol and deionized water. The resulting particles underwent an additional drying phase within a vacuum furnace, held at a temperature of 25°C, for a duration of eight hours.

Finding the RuCo@P/CNT nanocatalyst with the highest catalytic effect requires choosing the appropriate Ru, Co, and

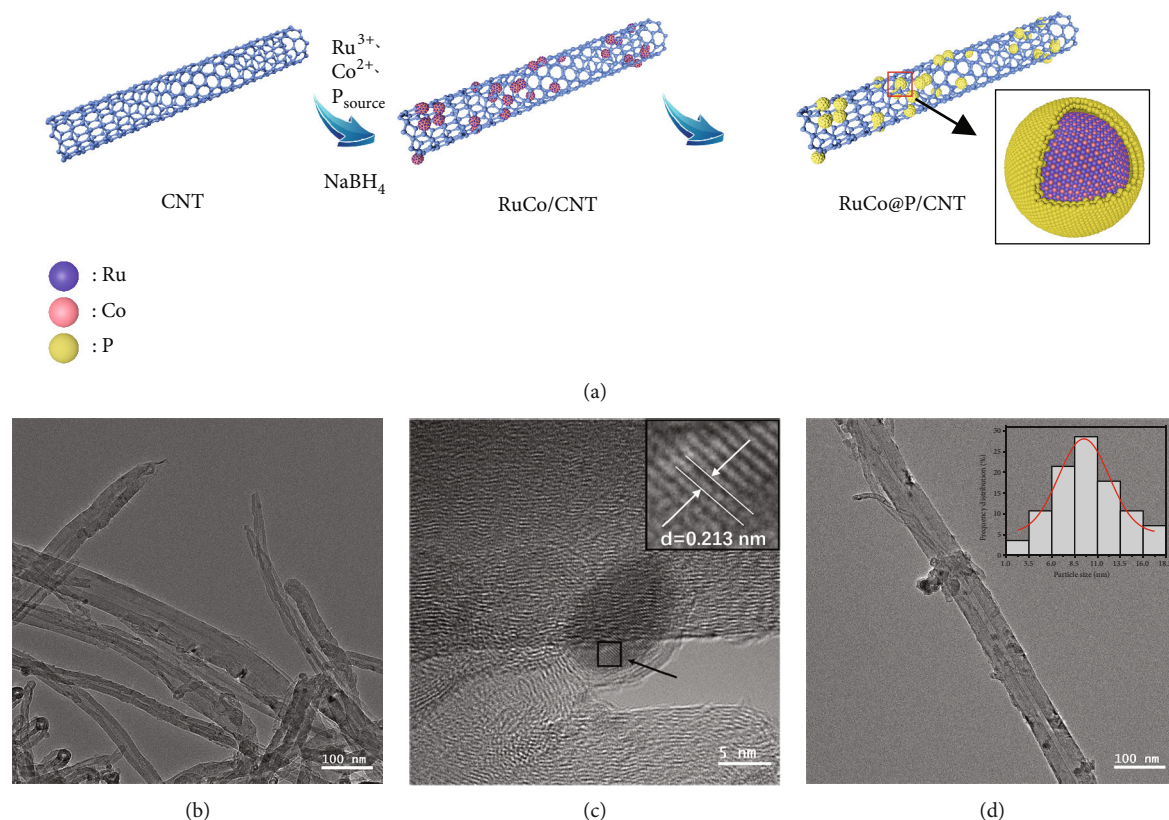


FIGURE 1: (a) Schematic diagram of the formation and the structure of RuCo@P/CNT NPs. (b, c) TEM images of Ru₁Co₁₀@P₅/CNT. (d) Size distribution of Ru₁Co₁₀@P₅/CNT.

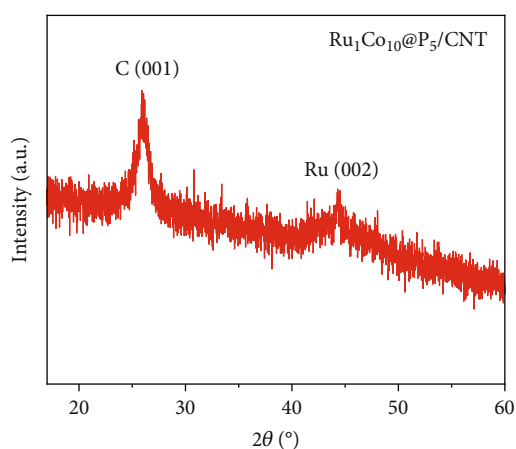


FIGURE 2: XRD images of Ru₁Co₁₀@P₅/CNT NPs.

P ratios. We synthesized RuCo@P/CNT nanoparticles with different material ratios by the same method as above under the condition of maintaining $n(\text{Ru}):n(\text{AB}) = 0.05$. The molar ratios of Co/Ru were altered across a range of values, including 0, 2.5, 5, 7.5, 10, 12.5, and 15. Similarly, the molar ratios of P/Ru were modified within the values of 2.5, 5, 7.5, 10, and 15.

2.3. Material Characterization. A JEM-1400Plus 120 kV transmission electron microscope was employed to capture

the TEM pictures. An Empyrean X-ray diffractometer scanning at a two angle between 5° and 80° was used to acquire XRD patterns. XPS spectra were acquired with a Thermo Scientific ESCALAB Xi+X-ray photoelectron spectroscopy. The element content was verified by ICP-OES (Prodigy 7). BET was scanned with the ASAP 2020 to test specific surface area and pore volume.

2.4. Catalytic Activity Tests. Ru₁Co₁₀@P₅/CNT catalyst was introduced to the reaction vessel, keeping its molar proportion of catalyst and AB constant, and four different temperatures, spanning from 298 K to 313 K, were carefully chosen to conduct the hydrolytic dehydrogenation reaction. Subsequently, the obtained experimental data were employed to calculate the reaction rate (k) as well as activation energy (E_a) for the catalyst through appropriate calculations and analysis. Similarly, we tested the number of reaction steps of ammonia borane-catalyzed hydrolytic dehydrogenation by changing the catalyst concentration value. The reaction temperature was set at 25°C and 1 mmol of AB was fixed.

To evaluate the cycling ability of the catalyst, the catalytic experiment is repeated five times with an equivalent quantity of AB added after each reaction. The turnover frequency (TOF) of the catalytic reaction was estimated using the formula shown below [11]:

$$\text{TOF} = \frac{PV/RT}{n_{\text{Ru}} * t}, \quad (2)$$

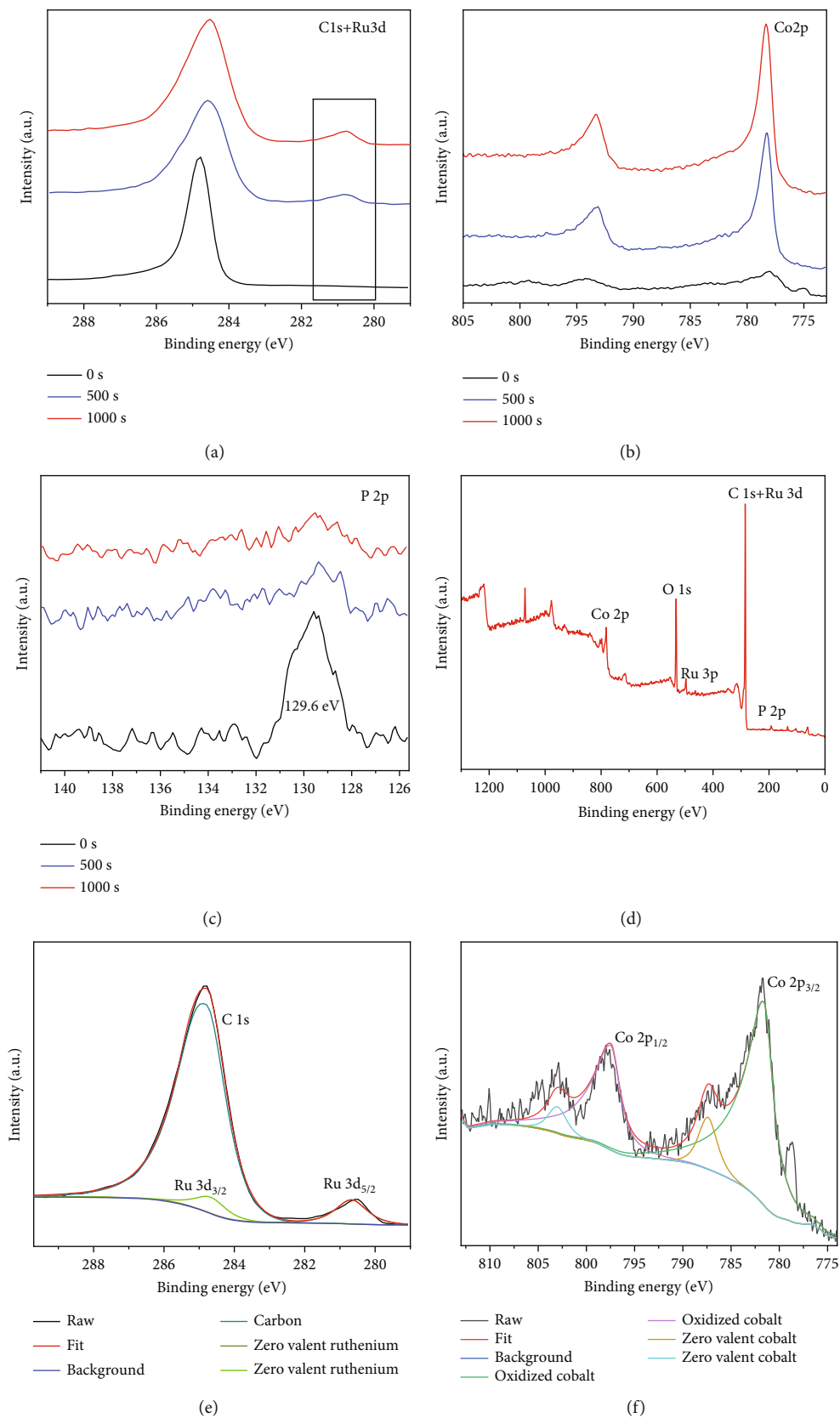
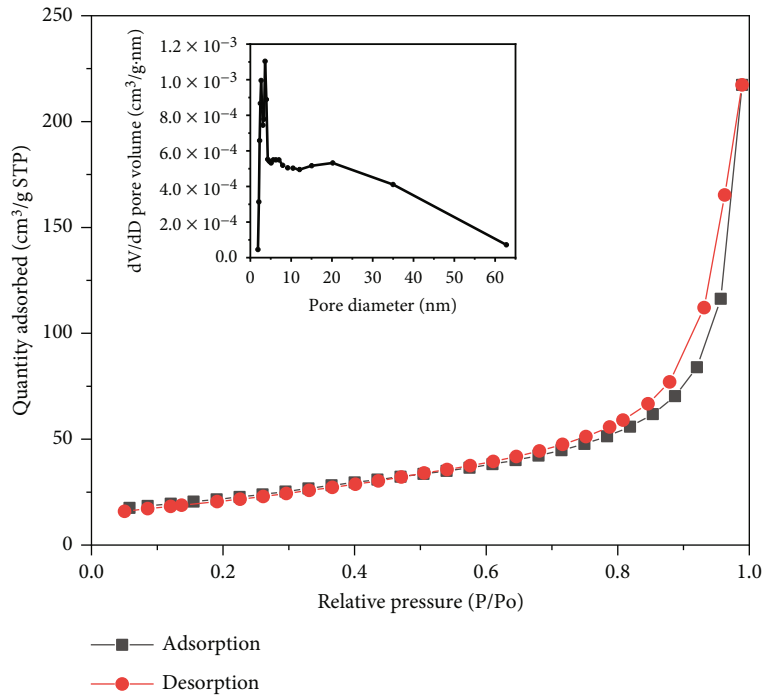
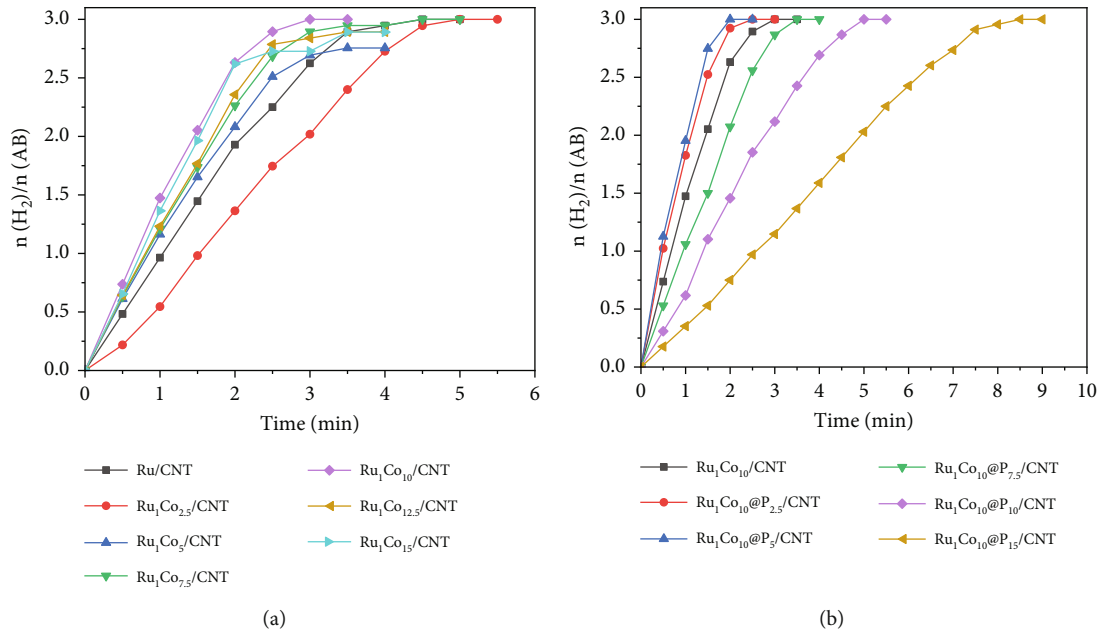


FIGURE 3: (a) XPS spectra of Ru 3d after etching for 0 s, 500 s, and 1000 s, respectively. (b) XPS spectra of Co 2p after etching for 0 s, 500 s, and 1000 s, respectively. (c) XPS spectra of P 2p after etching for 0 s, 500 s, and 1000 s, respectively. (d) XPS survey spectrum of Ru₁Co₁₀@P₅/CNT. (e) XPS spectra of Ru 3d. (f) XPS spectra of Co 2p.


 FIGURE 4: N_2 adsorption-desorption isotherm and pore size distribution image.

 FIGURE 5: (a) Hydrolysis of AB catalyzed by RuCo/CNT with different $n(\text{Ru}) : n(\text{Co})$. (b) Hydrolysis of AB catalyzed by RuCo@P/CNT with different $n(\text{Ru}) : n(\text{P})$ ($n(\text{Ru})/n(\text{AB}) = 0.005$).

where P denotes the ambient pressure, V denotes the volume of hydrogen production, R denotes the constant of molar gas, T denotes the reaction temperature, n_{Ru} denotes the molar quantity of Ru, and t denotes the reaction duration.

The reaction activation energy could be computed based on Arrhenius' reaction rate equation. After calculating its reaction rate at different temperature conditions, k is plotted against $1/T$, as shown in

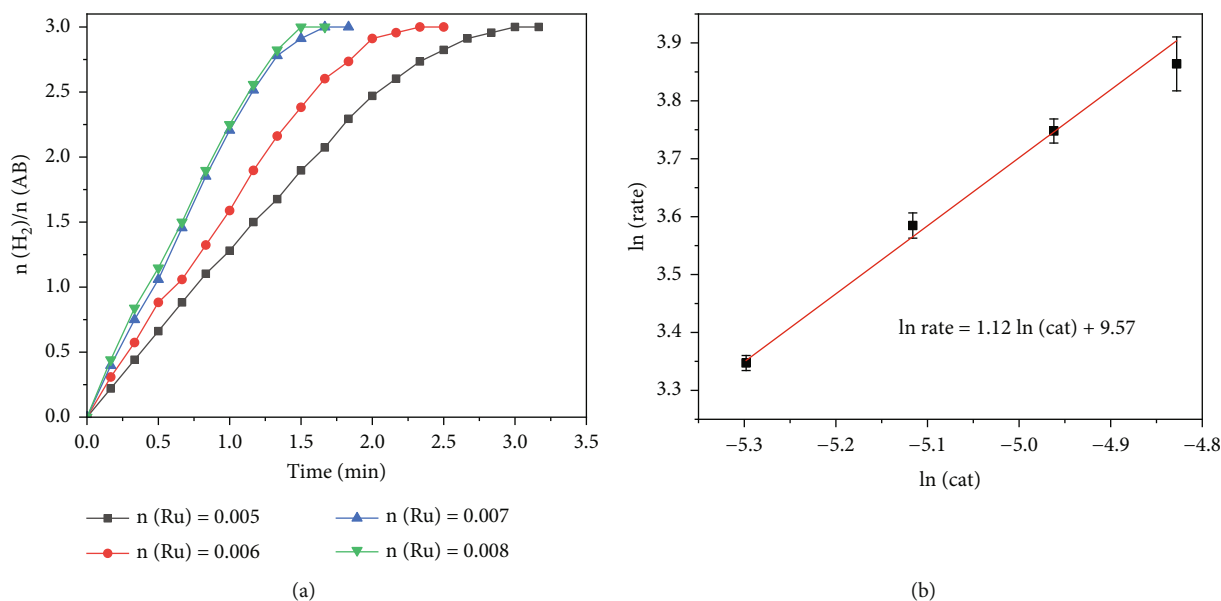
$$\ln k = \ln A - \frac{E_a}{RT}, \quad (3)$$

where A denotes the reaction constant.

In order to figure out the decisive step within the hydrolytic dehydrogenation of AB, the dehydrogenation experiments of AB were carried out with D_2O instead of H_2O , and the experimental conditions remained unchanged to

TABLE 1: Comparison of TOF and E_a of different catalysts for hydrogen generation from AB hydrolysis.

Catalyst	TOF (mol H ₂ m ol ⁻¹ M min ⁻¹) M = Pt, Ru, Pd, Ph	E_a (kJ mol ⁻¹)	Ref.
Ru@f-CNTs	764	35.68	[41]
Rh/CNTs	431	32	[42]
Ru@Co/graphene	344	/	[43]
Ru@Ni/graphene	339.5	36.59	[44]
Ru(0)@MWCNT	329	33	[45]
Ru ₁ Co ₁₀ @P ₅ /CNT	327.33	36.77	This study
Ru/g-C ₃ N ₄	313	37.4	[46]
Pt-Ru@PVP	308	56.3	[47]
Ru/TiO ₂	241	70	[48]
Ru@SiO ₂	200	38.2	[49]
Pd@Co@P/rGO	127.57	39.05	[11]
Ru@MIL-101	178	51.12	[50]
Ru/SiO ₂ -CoFe ₂ O ₄	172	45.6	[51]
RuCu/graphene	135	30.39	[52]
Ru@X-NW	135	77	[53]
Co	44.2	/	[54]
Co-P (at 30°C)	10	22	[55]

FIGURE 6: (a) Time plots of catalytic dehydrogenation of AB catalyzed by Ru₁Co₁₀@P₅/CNT at different catalyst concentrations. (b) Logarithmic plot of hydrogen generation rate versus the concentration of Ru₁Co₁₀@P₅/CNT.

obtain the graphs of the dehydrogenation of AB catalyzed by both, respectively. The linear part of the reactions was taken to calculate the reaction rate k , and the kinetic isotope effect values (k_{H_2O}/k_{D_2O}) were obtained by comparison.

3. Results and Discussions

3.1. Characterization. By adding NaBH₄ to the solution of RuCl₃, CoCl₂, NaH₂PO₂, and CNT at room temperature,

we obtained CNT-loaded RuCo@P NPs. NaH₂PO₂ is a kind of weak Bronsted acid, and when the content is high, it will easily hydrolyze to produce NaOH [29]. The reducibility of NaBH₄ sodium borohydride will be reduced in the presence of NaOH [30]. Therefore, the reduction sequence of metal ions is changed, providing conditions for forming a core-shell structure with higher catalytic activities with stronger stabilities [25, 31, 32]. Ru³⁺ has the highest reduction potential of the three ions (E^0 (Ru³⁺/Ru) = +0.40 eV vs. SHE),

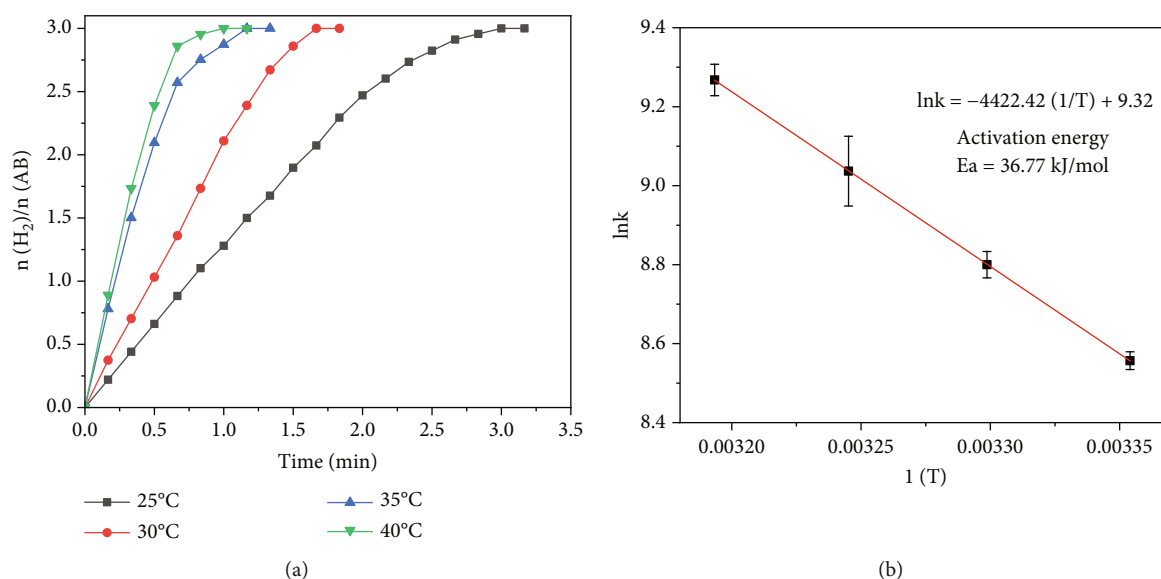


FIGURE 7: (a) Time plots of catalytic dehydrogenation of AB catalyzed by Ru₁Co₁₀@P₅/CNT at 25-40°C. (b) Arrhenius plot obtained from the data in Figure 7(a).

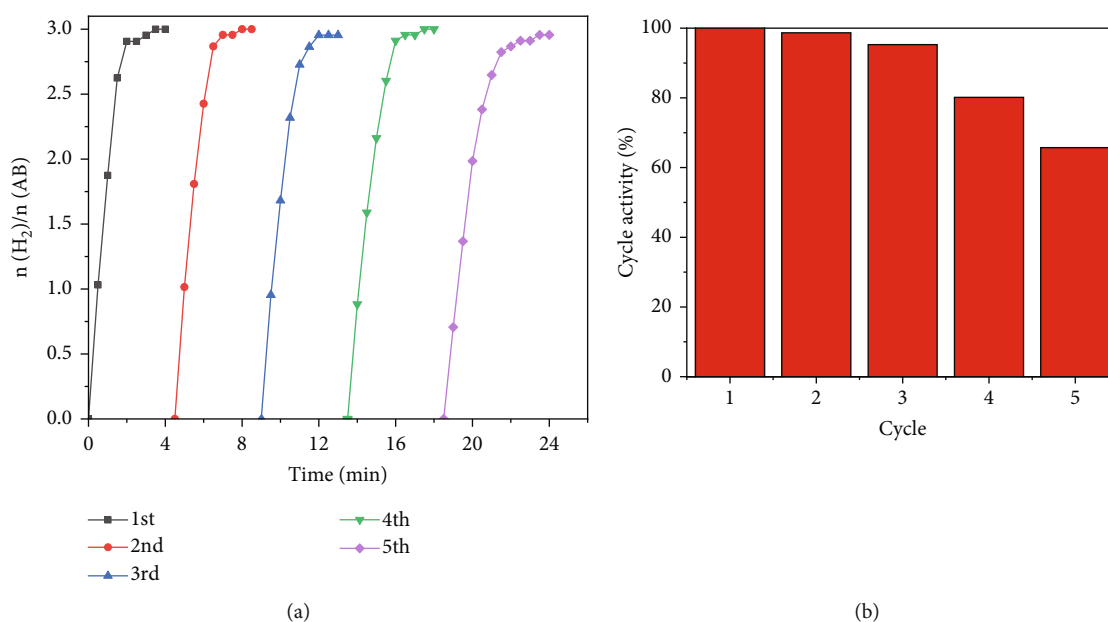


FIGURE 8: (a) Time plots of catalytic dehydrogenation of AB catalyzed by Ru₁Co₁₀@P₅/CNT for five cycles. (b) Histogram of catalytic activity as a percentage of initial activity after each cycle.

followed by Co²⁺ ($E^0(\text{Co}^{2+}/\text{Co}) = -0.28$ eV vs. SHE), and H₂PO₂⁻ has the lowest reduction potential ($E^0(\text{H}_2\text{PO}_2^-/\text{P}) = -0.508$ eV vs. SHE). Due to the reduction of the reducibility of NaBH₄, Ru³⁺ and Co²⁺ with higher reduction potential were reduced firstly as the core. The formed M-H (M = Ru, Co) with strong reducibility reduced the H₂PO₂⁻ with the lowest reduction potential subsequently to form the shell. Figure 1(a) shows the formation process of the RuCo@P/CNT NPs.

Transmission electron microscopy (TEM) was used to examine the catalyst's morphological properties and the

microstructure pictures of Ru₁Co₁₀@P₅/CNT shown in Figures 1(b) and 1(c). As shown in Figure 1(b), Ru₁Co₁₀@P₅/CNT nanoparticles are uniformly distributed on the carbon nanotubes, which indicates that the carbon nanotubes can well prevent the aggregation of nanoparticles. The wall stripe of the carbon nanotube is visible in Figure 1(c). The Ru₁Co₁₀@P₅ nanoparticle on CNT has a core-shell structure, and the core part is measured to have a lattice stripe of 0.213 nm, which is identified as the crystal plane of Ru (002), indicating that Ru³⁺ was reduced firstly due to its high electric potential. The absence of lattice

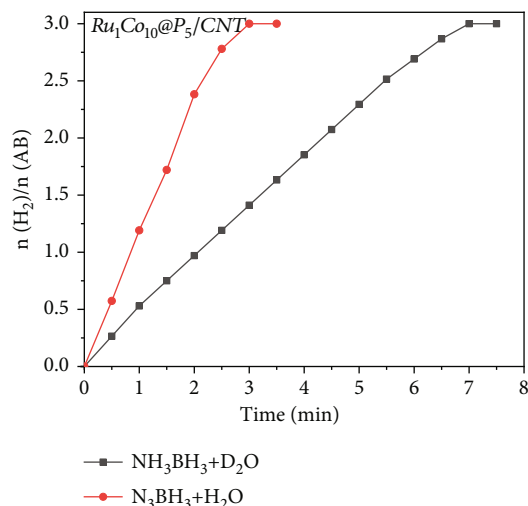


FIGURE 9: Evolution of H_2 from NH_3BH_3 hydrolysis with H_2O and D_2O as the solvent catalyzed by $\text{Ru}_1\text{Co}_{10}@P_5/\text{CNT}$ (KIE = 2.61).

stripes in Co is probably related to the fact that it often exists in an amorphous form. Figure 1(d) shows the particle size distribution of $\text{Ru}_1\text{Co}_{10}@P_5/\text{CNT}$ nanoparticles, which was measured to have an average particle size of 8.9 nm.

Figure 2 shows the XRD pattern of $\text{Ru}_1\text{Co}_{10}@P_5/\text{CNT}$ after calcination. The peaks at 26° and 44.3° correspond to the C (001) and Ru (002) (PDF#06-0663) crystalline plane of $\text{Ru}_1\text{Co}_{10}@P_5/\text{CNT}$ products, respectively. The XRD results do not show peaks of Co and P, indicating that Co and P exist in the amorphous form [11], which is also consistent with the TEM results.

The precise chemical makeup and electronic states of the $\text{Ru}_1\text{Co}_{10}@P_5/\text{CNT}$ catalysts and the synthesis mechanism were further clarified using X-ray photoelectron spectroscopy (XPS). Figures 3(a)–3(c) show the XPS spectra of Ru, Co, and P elements after etching for 0 s, 500 s, and 1000 s, respectively. Due to the interference of the C 1s peak, the peak around 285 eV cannot be used as a reference basis for judging the elemental content, and it can be seen that there is no Ru $3d_{5/2}$ peak on the surface of nanoparticles in Figure 3(a). After 500 s and 1000 s of surface etching, the material on the nanoparticles' surface is removed, while the peak at around 280.2 eV appears. It can be judged that the metal Ru does not exist in the outermost layer of the nanoparticles but is basically distributed in the core part, and it is also consistent with the lattice spacing measured in the TEM imaging. Similarly, according to Figure 3(b), the XPS spectra of Co 2p can be seen that after 500 s and 1000 s of surface etching, the peaks of Co $2p_{1/2}$ and Co $2p_{3/2}$ appear significantly enhanced in height and area. It can be judged that only a small amount of Co exists on the surface of the nanoparticles, and most of it is distributed in the core part, like Ru. In addition, according to the elemental content analysis of the XPS outcomes, the atomic content of Ru and Co within the sample increased by 20% and 30%, respectively, after 1000 s of etching compared with that before etching, which indicates that the Ru and Co elements increased significantly during the etching process. This further confirms

that Ru and Co are preferentially reduced and attached to the CNT in the form of a core, guiding P with lower reduction potential to be coated on the surface in the form of a shell. Moreover, since the TEM images show the lattice spacing of the inner layer of nanoparticles is Ru, it can be concluded that Co primarily exists in an amorphous form.

In Figure 3(c) (XPS pattern of P 2p), it can be seen that the characteristic peak of P 2p at 129.6 eV appears at 0 s of etching, indicating the oxidation of P to form P^{3+} during the sample preparation. After 500 s of surface etching, the characteristic peak at 129.6 eV has been less prominent, and after 1000 s of surface etching, the characteristic peak at 129.6 eV has almost disappeared, which further indicates that the P element is distributed in the outermost layer of this nanoparticle, which coincides with TEM outcomes.

The outcomes of TEM, XRD, and XPS reveal that the reduction sequence changes due to the reduced NaBH_4 , Ru^{3+} ($E^0(\text{Ru}^{3+}/\text{Ru}) = +0.40$ eV vs. SHE), and Co^{2+} ($E^0(\text{Co}^{2+}/\text{Co}) = -0.28$ eV vs. SHE) are first reduced to RuCo alloy nanoparticles due to the relatively high reduction potential and then used as in situ seeds, inducing the formation of RuCo-H, a highly reducing intermediate. The generated RuCo-H then reduces H_2PO_2^- ($E^0(\text{H}_2\text{PO}_2^-/\text{P}) = -0.508$ eV vs. SHE) exhibiting the potential of low reduction to P^0 , so that P, as the shell in the core shell, continuously grows on the surface with RuCo alloy as the core.

The entire spectrum of $\text{Ru}_1\text{Co}_{10}@P_5/\text{CNT}$ (Figure 3(d)) clearly shows the presence of Ru, Co, P, C, and O, which indicates that Ru, Co, and P are successfully loaded on the carbon nanotubes. The prominent Ru peak in the zero-valence state can be seen in Figure 3(e), indicating that the metal Ru is stable as a core. However, due to the close closeness of the C 1s and Ru 3d peaks at 284.5 eV, it took work to corroborate the existence of Ru. Contrarily, the XPS survey scan revealed a clear Ru 3p peak at around 463 eV, indicating the presence of Ru. Two peaks at 781.7 eV and 797.6 eV in the spectrum, which represent zero-valent Co, and two peaks at 787.3 eV and 803.1 eV, which represent the oxidized state of Co, are shown as the peaks of Co 2p in Figure 3(f). The outcomes suggest that partial oxidation of Co may have occurred during the synthesis and catalysis of the sample leading to the production of the oxidized state of Co [33, 34].

The textural properties of the nanoparticles were further tested by BET. The introduction of the CNT can appreciably increase BET surface area and mesopore volume of the nanoparticles [35]. Figure 4 shows the nitrogen adsorption curve of $\text{Ru}_1\text{Co}_{10}@P_5/\text{CNT}$ sample calculated using the BET model, and the material displays a typical type IV behavior, indicating that the $\text{Ru}_1\text{Co}_{10}@P_5/\text{CNT}$ NPs occupy the orifice of the CNT. The surface area of $\text{Ru}_1\text{Co}_{10}@P_5/\text{CNT}$ was calculated to be $72.528 \text{ m}^2\cdot\text{g}^{-1}$ using the Brunauer-Emmett-Teller (BET) model [36]. The average pore size is 17.13 nm, concentrated at 2–20 nm, and determined as a mesoporous material.

3.2. Catalytic Activity of RuCo@P/CNT NPs. We synthesized several RuCo@P/CNT catalysts by adjusting the proportions of the three components and investigated the catalytic

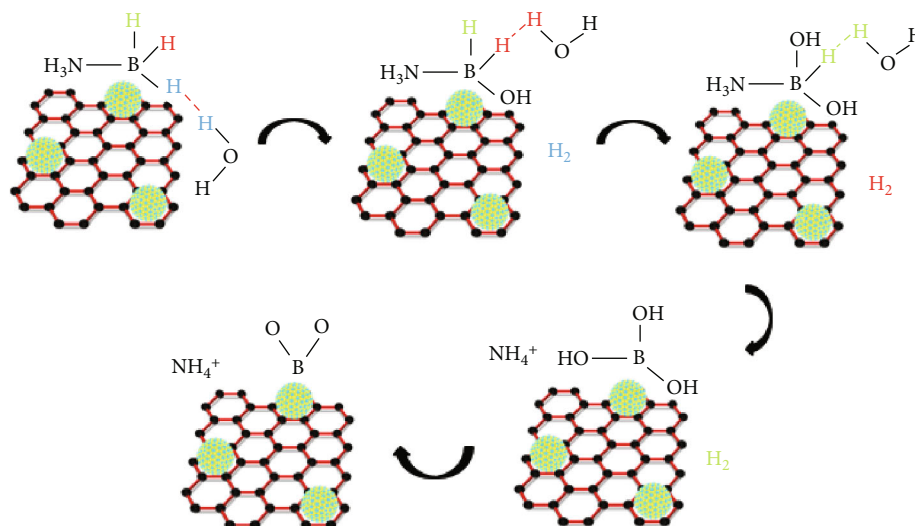


FIGURE 10: The reaction mechanism of hydrolysis dehydrogenation of ammonia borane catalyzed by $\text{Ru}_1\text{Co}_{10}\text{@P}_5/\text{CNT}$.

performance of each catalyst for AB hydrolysis separately. As illustrated in Figure 5(a), when the molar proportion of Ru to AB was maintained at 0.005, if no Co element was added, Ru/CNT catalyzed the total hydrolysis of AB in about 4.5 min. When the Co/Ru ratio was increased to 10, the decomposition of AB was completed in 3 min, and further increasing the Co/Ru ratio to 15 led to a prolonged reaction duration, indicating that the RuCo/CNT nanoparticles had a promoting effect on the hydrolysis of AB, while the optimal proportion of Co/Ru was 10. On this basis, the amount of phosphorus was varied by changing the amount of NaH_2PO_2 when P was selected for addition to the catalyst RuCo/CNT NPs. As revealed in Figure 5(b), the entire breakdown of AB through hydrolysis can be achieved within approximately 3 min by utilizing $\text{Ru}_1\text{Co}_{10}\text{@P}_5/\text{CNT}$ as a catalyst while maintaining a consistent proportion of Ru to AB at 0.005, while the proportion of AB hydrolysis via catalysis was markedly enhanced subsequent to the introduction of P doping. Notably, the catalytic performance peaked when the P/Ru ratio was increased to 10, leading to the completion of the reaction in just 2 min, accompanied by a turnover frequency of 327.33 min^{-1} . This TOF value surpasses numerous Ru-based and other noble metal catalysts outlined in Table 1. However, as the P content was further increased, and the catalytic activity experienced a decline. Finally, the $\text{Ru}_1\text{Co}_{10}\text{@P}_5/\text{CNT}$ catalyst exhibiting the highest catalytic activity was obtained. The mass loading of RuCo@P/CNT nanoparticles and on reduced CNT is 33.98 wt% which is calculated from the results of ICP-OES. In addition, the Ru content was determined to be 2.19 wt%, the Co content was determined to be 21.85 wt%, and the P content was determined to be 9.95 wt% by ICP-OES. The ICP-OES results showed that the content of Ru, Co, and P elements was 1:9.98:4.54, and the slightly lower P element ratio should be the decrease in purity caused by the dampness of NaH_2PO_2 , with an error within an acceptable range.

After identifying the RuCo@P/CNT nanoparticles that exhibited the most effective catalytic performance, further investigation was conducted to examine the reaction kinetics

of the catalytic dehydrogenation process using the $\text{Ru}_1\text{Co}_{10}\text{@P}_5/\text{CNT}$ catalyst. Figure 6(a) presents the experimental outcomes obtained by varying the Ru concentrations ($n(\text{Ru}) = 0.05, 0.06, 0.07, \text{ and } 0.08$). At a steady temperature of 25°C , 1 mmol of ammonia borane was added. The dehydrogenation rate constant (k) was calculated using the linear section of the curve. For a linear fit, we performed a logarithmic transformation of the catalyst concentration. As seen in Figure 6, the slope of the fitted curve was 1.12, indicating a first-order reaction mechanism for the hydrolysis of ammonia borane with the catalyst.

A suitable catalyst can effectively reduce the E_a of a chemical reaction, thus promoting the reaction products to reach the activated state and increasing the proportion of the reaction. Figure 7(a) shows the catalytic tests with $\text{Ru}_1\text{Co}_{10}\text{@P}_5/\text{CNT}$ catalyst at various temperatures (298, 303, 308, and 313 K). According to the Arrhenius formula, we must perform a logarithmic fit to the rate constant and the inverse of the temperature for the dehydrogenation reaction. By choosing the linear part of the experimental curve, we can calculate the rate constant k and obtain the fitting outcomes shown in Figure 7(b). The outcomes revealed that the E_a of $\text{Ru}_1\text{Co}_{10}\text{@P}_5/\text{CNT}$ catalyst was $36.77 \text{ kJ}\cdot\text{mol}^{-1}$, which was better than most of the reported ruthenium-containing catalysts (Table 1), indicating that our synthesized $\text{Ru}_1\text{Co}_{10}\text{@P}_5/\text{CNT}$ catalyst had suitable catalytic activities.

To decrease the frequency of catalyst replacements in actual practice, it is necessary to ensure a high degree of cycling stability of the catalyst. The cycling stability of $\text{Ru}_1\text{Co}_{10}\text{@P}_5/\text{CNT}$ in catalytic AB hydrolysis is shown in Figure 8. $\text{Ru}_1\text{Co}_{10}\text{@P}_5/\text{CNT}$ nanoparticles maintained 65.74% of the initial catalytic activity following the catalytic hydrolysis of ammonia borane for five consecutive cycles. In addition, the hydrogen conversion was also well maintained, indicating that $\text{Ru}_1\text{Co}_{10}\text{@P}_5/\text{CNT}$ nanoparticles can be cycled at least five times and possess good cycling performance.

To further investigate the hydrolysis mechanism of $\text{Ru}_1\text{Co}_{10}\text{@P}_5/\text{CNT}$ -catalyzed ammonia borane, isotope experiments were conducted using D_2O and H_2O as reaction

solutions, respectively (Figure 9). The dehydrogenation rate of ammonia borane in D_2O was substantially lower than in H_2O . This difference may be related to the higher molecular mass of D_2O , which needs more energy to break chemical bonds. Indirect evidence from this phenomenon supports the primary role of this reaction in the O-H bond breakage of water. The linear portion of the corresponding reaction curves was computed to produce the reaction rate constant k , and the kinetic isotope effect value (k_{H_2O}/k_{D_2O}) was determined to be 2.61. This finding demonstrates the existence of a first-order kinetic isotope effect. It confirms that the synergistic catalytic breakage of the H-OH bond in water is the critical rate step in the hydrolysis of AB rather than the H-BH₂NH₃ bond. Combining the results, we can deduce the mechanism of Ru₁Co₁₀P₅/CNT-catalyzed hydrolysis of ammonia borane [7, 37, 38], shown in Figure 10.

The surface of the RuCo@P nanoparticles is simultaneously bound to and activated in the earliest stages of the process when H_2O molecules form the structure [H₃NBH₂H]•••H-OH [39] with AB. The B-H bond is initially cleaved during the activation process, while RuCo@P nanoparticles adsorb the H atoms in the B-H bond under synergistic effects. At the same time, the water molecule undergoes a continuous O-H break, in which the OH⁻ replaces an H atom in the AB. Thus, NH₃BH₃ and H_2O each provide an active H atom, which combines to form the product H₂, while the reaction also produces the by-products BH(OH)₂NH₃ and B(OH)₃ [40].

4. Conclusion

Summarily, transition metal phosphide-based core-shell Ru₁Co₁₀@P₅/CNT catalysts were successfully synthesized in this study. We thoroughly investigated the catalytic activity, catalytic mechanism, and cyclic performance of the catalysts in the hydrolytic dehydrogenation of ammonia borane. The experimental outcomes revealed that NaBH₄ was reduced by the hydrolysis of NaH₂PO₂, leading to the formation of RuCo core from Ru³⁺ ions and Co²⁺ ions and prompting H₂PO₂⁻ reduction, which resulted in the growth of the shell. The Ru₁Co₁₀@P₅/CNT catalyst exhibited an excellent conversion frequency (TOF) of 327.33 min⁻¹ and activation energy of 36.77 kJ·mol⁻¹, exhibiting excellent catalytic activity and cycling stability in the catalytic process. Moreover, few researchers have studied the catalytic effect of the combination of Ru, Co, and P on AB before this. The results indicate that Co doping can effectively improve the performance of Ru-based metal catalysts while reducing catalyst costs. The introduction of P alters the electronic structure between Ru and Co metal elements, making it easier for H to be adsorbed and desorbed on the surface of the nanoparticles, resulting in RuCo@P/CNT having superior performance compared to other Ru-based catalysts, and this simple synthesis method can be extended to other Ru-based bimetallic core-shell systems for wider applications.

This simple one-pot synthesis method can be used to synthesize other metal phosphide catalysts and further apply in the dehydrogenation of AB.

Data Availability

The data that support the findings of this study are available from the corresponding author upon reasonable request.

Conflicts of Interest

The authors declare that they have no conflicts of interest.

Acknowledgments

We acknowledge the financial support of the Natural Science Foundation of Hubei Province (Grant No. 20231j0195), the National Natural Science Foundation of China (Grant No. 21805217), and the Fundamental Research Funds for the Central Universities (WUT: 2019IVB014 and 2021IVA014) for this research.

References

- [1] Y. Karataş, T. Çetin, Y. Akinay, and M. Gülcan, "Synthesis and characterization of Pd doped MXene for hydrogen production from the hydrolysis of methylamine borane: effect of cryogenic treatment," *Journal of the Energy Institute*, vol. 109, article 101310, 2023.
- [2] Y. Karataş, T. Çetin, İ. N. Akkuş, Y. Akinay, and M. Gülcan, "Rh (0) nanoparticles impregnated onto two-dimensional transition metal carbides, MXene, as an effective nanocatalyst for ammonia-borane hydrolysis," *International Journal of Hydrogen Energy*, vol. 46, no. 8, pp. 11411–11423, 2022.
- [3] M.-J. Valero-Pedraza, A. Martín-Cortés, A. Navarrete, M. D. Bermejo, and Á. Martín, "Kinetics of hydrogen release from dissolutions of ammonia borane in different ionic liquids," *Energy*, vol. 91, pp. 742–750, 2015.
- [4] H. K. Cai, L. P. Liu, Q. Chen, P. Lu, and J. Dong, "Ni-polymer nanogel hybrid particles: a new strategy for hydrogen production from the hydrolysis of dimethylamine-borane and sodium borohydride," *Energy*, vol. 99, pp. 129–135, 2016.
- [5] R. M. Fang, Z. Q. Yang, Z. Q. Wang, J. Y. Ran, Y. F. Yan, and L. Zhang, "Novel non-noble metal catalyst with high efficiency and synergetic photocatalytic hydrolysis of ammonia borane and mechanism investigation," *Energy*, vol. 244, p. 123187, 2022.
- [6] D. Katla, M. Jurczyk, A. Skorek-Osikowska, and W. Uchman, "Analysis of the integrated system of electrolysis and methanation units for the production of synthetic natural gas (SNG)," *Energy*, vol. 237, article 121479, 2021.
- [7] M. H. Fang, S. Y. Wu, Y. H. Chang et al., "Mechanistic insight into the synergetic interaction of ammonia borane and water on ZIF-67-derived Co@porous carbon for controlled generation of dihydrogen," *ACS Applied Materials & Interfaces*, vol. 13, no. 40, pp. 47465–47477, 2021.
- [8] S. Akbayrak, Y. Tonbul, and S. Özkar, "Ceria supported rhodium nanoparticles: superb catalytic activity in hydrogen generation from the hydrolysis of ammonia borane," *Applied Catalysis*, vol. 198, pp. 162–170, 2016.
- [9] J. Manna, S. Akbayrak, and S. Özkar, "Nickel(0) nanoparticles supported on bare or coated cobalt ferrite as highly active, magnetically isolable and reusable catalyst for hydrolytic dehydrogenation of ammonia borane," *Journal of Colloid and Interface Science*, vol. 508, pp. 359–368, 2017.

- [10] H. T. Zou, F. Guo, M. H. Luo, Q. L. Yao, and Z. H. Lu, "La(OH)₃-decorated NiFe nanoparticles as efficient catalyst for hydrogen evolution from hydrous hydrazine and hydrazine borane," *International Journal of Hydrogen Energy*, vol. 45, no. 20, pp. 11641–11650, 2020.
- [11] B. Qu, Y. Tao, L. Yang, and Y. H. Liu, "One-pot co-reduction synthesis of orange-like Pd@Co@P nanoparticles supported on rGO for catalytic hydrolysis of ammonia borane," *International Journal of Hydrogen Energy*, vol. 46, no. 61, pp. 31324–31333, 2021.
- [12] B. Xia, T. Liu, W. Luo, and G. Z. Cheng, "NiPt-MnO_x supported on N-doped porous carbon derived from metal-organic frameworks for highly efficient hydrogen generation from hydrazine," *Journal of Materials Chemistry A*, vol. 4, no. 15, pp. 5616–5622, 2016.
- [13] C. Menghuan, L. Zhou, L. Di et al., "RuCo bimetallic alloy nanoparticles immobilized on multi-porous MIL-53(Al) as a highly efficient catalyst for the hydrolytic reaction of ammonia borane," *International Journal of Hydrogen Energy*, vol. 43, no. 3, pp. 1439–1450, 2018.
- [14] G. P. Rachiero, U. B. Demirci, and P. Miele, "Bimetallic RuCo and RuCu catalysts supported on γ -Al₂O₃. A comparative study of their activity in hydrolysis of ammonia-borane," *International Journal of Hydrogen Energy*, vol. 36, no. 12, pp. 7051–7065, 2011.
- [15] G. Z. Chen, S. Desinan, R. Rosei, F. Rosei, and D. L. Ma, "Synthesis of Ni-Ru alloy nanoparticles and their high catalytic activity in dehydrogenation of ammonia borane," *Chemistry - A European Journal*, vol. 18, no. 25, pp. 7925–7930, 2012.
- [16] X. K. Huang, X. Wang, P. B. Jiang et al., "Ultrasmlal MoP encapsulated in nitrogen-doped carbon hybrid frameworks for highly efficient hydrogen evolution reaction in both acid and alkaline solutions," *Inorganic Chemistry Frontiers*, vol. 6, no. 6, pp. 1482–1489, 2019.
- [17] R. Hamiye, C. Lancelot, P. Blanchard, J. Toufaily, T. Hamieh, and C. Lamonnier, "Diesel HDS performance of alumina supported CoMoP catalysts modified by sulfone molecules produced by ODS process," *Fuel*, vol. 210, pp. 666–673, 2017.
- [18] W. Liu, W. Y. Tan, H. W. He, Y. Z. Peng, Y. X. Chen, and Y. Yang, "One-step electrodeposition of Ni-Ce-Pr-Ho/NF as an efficient electrocatalyst for hydrogen evolution reaction in alkaline medium," *Energy*, vol. 250, article 123831, 2022.
- [19] J. G. Yang, Q. Yuan, Y. Liu et al., "Low-cost ternary Ni-Fe-P catalysts supported on Ni foam for hydrolysis of ammonia borane," *Inorganic Chemistry Frontiers*, vol. 6, no. 5, pp. 1189–1194, 2019.
- [20] C. Wang, Z. L. Wang, H. L. Wang et al., "Noble-metal-free Co@Co₂P/N-doped carbon nanotube polyhedron as an efficient catalyst for hydrogen generation from ammonia borane," *International Journal of Hydrogen Energy*, vol. 46, no. 13, pp. 9030–9039, 2021.
- [21] X. P. Qu, R. Jiang, Q. Li et al., "The hydrolysis of ammonia borane catalyzed by NiCoP/OPC-300 nanocatalysts: high selectivity and efficiency, and mechanism," *Green Chemistry*, vol. 21, no. 4, pp. 850–860, 2019.
- [22] M. Asim, B. Maryam, S. Zhang et al., "Synergetic effect of Au nanoparticles and transition metal phosphides for enhanced hydrogen evolution from ammonia-borane," *Journal of Colloid and Interface Science*, vol. 638, pp. 14–25, 2023.
- [23] C. Wan, G. Li, J. Wang et al., "Modulating electronic metal-support interactions to boost visible-light-driven hydrolysis of ammonia borane: nickel-platinum nanoparticles supported on phosphorus-doped titania," *Angewandte Chemie, International Edition*, vol. 62, no. 40, article e202305371, 2023.
- [24] H. Wu, Y. J. Cheng, Y. P. Fan et al., "Metal-catalyzed hydrolysis of ammonia borane: mechanism, catalysts, and challenges," *International Journal of Hydrogen Energy*, vol. 45, no. 55, pp. 30325–30340, 2020.
- [25] M. U. Gürbüz, G. Elmacı, and A. S. Ertürk, "In situ deposition of silver nanoparticles on polydopamine-coated manganese ferrite nanoparticles: synthesis, characterization, and application to the degradation of organic dye pollutants as an efficient magnetically recyclable nanocatalyst," *Applied Organometallic Chemistry*, vol. 35, no. 8, article e6284, 2021.
- [26] Q. T. Wang, Z. Zhang, J. Liu, R. C. Liu, and T. Liu, "Bimetallic non-noble CoNi nanoparticles monodispersed on multiwall carbon nanotubes: highly efficient hydrolysis of ammonia borane," *Materials Chemistry and Physics*, vol. 204, pp. 58–61, 2018.
- [27] B. T. Liu, Y. L. Xu, S. Y. Zhang et al., "FeCo alloy encapsulated within carbon nanotube as efficient and stable catalyst for ammonia borane hydrolysis," *Materials Letters*, vol. 239, pp. 124–127, 2019.
- [28] W. Y. Chen, D. L. Li, C. Peng et al., "Mechanistic and kinetic insights into the Pt-Ru synergy during hydrogen generation from ammonia borane over PtRu/CNT nanocatalysts," *Journal of Catalysis*, vol. 356, pp. 186–196, 2017.
- [29] V. Alisoglu and G. Nedzhefoglu, "Phase equilibria in the system NaNO₃-NaH₂PO₄-Mn(H₂PO₄)₂-H₂O at 25°C," *Zhurnal Neorganicheskoi Khimii*, vol. 43, pp. 1732–1733, 1998.
- [30] S. I. Shabunya and A. A. Nesteruk, "Hydrolysis of aqueous-alkaline solutions of sodium borohydride. Asymptotics of low concentrations of the alkali," *Journal of Engineering Physics and Thermophysics*, vol. 85, no. 1, pp. 73–78, 2012.
- [31] P. Eghbali, M. U. Gürbüz, A. S. Ertürk, and Ö. Metin, "In situ synthesis of dendrimer-encapsulated palladium(0) nanoparticles as catalysts for hydrogen production from the methanolysis of ammonia borane," *International Journal of Hydrogen Energy*, vol. 45, no. 49, pp. 26274–26285, 2020.
- [32] A. S. Ertürk, G. Elmacı, and M. U. Gürbüz, "Reductant free green synthesis of magnetically recyclable MnFe₂O₄@SiO₂-Ag core-shell nanocatalyst for the direct reduction of organic dye pollutants," *Turkish Journal of Chemistry*, vol. 45, no. 6, pp. 1968–1979, 2021.
- [33] C. Wang, Y. Zhang, X. Sun et al., "Preparation of Pd/PdO loaded WO₃ microspheres for H₂S detection," *Sensors and Actuators B: Chemical*, vol. 321, article 128629, 2020.
- [34] H. B. Hu, B. Long, Y. F. Jiang et al., "Synthesis of a novel Co-B/CTAB catalyst via solid-state-reaction at room temperature for hydrolysis of ammonia-borane," *Chemical Research in Chinese Universities*, vol. 36, no. 6, pp. 1209–1216, 2020.
- [35] T.-V. Reshetenko, H.-T. Kim, and H.-J. Kweon, "Modification of cathode structure by introduction of CNT for air-breathing DMFC," *Electrochimica Acta*, vol. 53, no. 7, pp. 3043–3049, 2008.
- [36] L. Yang, Z. Liu, B. Qu, Y. Tao, and Y. Liu, "Highly efficient dehydrogenation of ammonia borane over reduced graphene oxide-supported Pd@NiP nanoparticles at room temperature," *International Journal of Energy Research*, vol. 2023, Article ID 9889312, 13 pages, 2023.
- [37] N. Kang, Q. Wang, R. Djeda et al., "Visible-light acceleration of H₂ Evolution from aqueous solutions of inorganic hydrides

- catalyzed by gold-transition-metal nanoalloys,” *ACS Applied Materials & Interfaces*, vol. 12, no. 48, pp. 53816–53826, 2020.
- [38] Q. Wang, F. Fu, S. Yang et al., “Dramatic synergy in CoPt nanocatalysts stabilized by “click” dendrimers for evolution of hydrogen from hydrolysis of ammonia borane,” *ACS Catalysis*, vol. 9, no. 2, pp. 1110–1119, 2019.
- [39] U. B. Demirci, “Mechanistic insights into the thermal decomposition of ammonia borane, a material studied for chemical hydrogen storage,” *Inorganic Chemistry Frontiers*, vol. 8, no. 7, pp. 1900–1930, 2021.
- [40] Y. He, Y. Peng, Y. Wang, Y. Long, and G. Fan, “Air-engaged fabrication of nitrogen-doped carbon skeleton as an excellent platform for ultrafine well-dispersed RuNi alloy nanoparticles toward efficient hydrolysis of ammonia borane,” *Fuel*, vol. 297, article 120750, 2021.
- [41] A. Guo, L. Hu, Y. M. Peng et al., “Steam pretreatment-mediated catalytic activity modulation for ammonia borane hydrolysis over ruthenium nanoclusters on nitrogen/oxygen-rich carbon nanotubes,” *Applied Surface Science*, vol. 579, article 152158, 2022.
- [42] Q. Yao, Z. H. Lu, Y. Jia, X. Chen, and X. Liu, “In situ facile synthesis of Rh nanoparticles supported on carbon nanotubes as highly active catalysts for H₂ generation from NH₃BH₃ hydrolysis,” *International Journal of Hydrogen Energy*, vol. 40, no. 5, pp. 2207–2215, 2015.
- [43] N. Cao, J. Su, W. Luo, and G. Z. Cheng, “Graphene supported Ru@Co core-shell nanoparticles as efficient catalysts for hydrogen generation from hydrolysis of ammonia borane and methylamine borane,” *Catalysis Communications*, vol. 43, pp. 47–51, 2014.
- [44] N. Cao, J. Su, W. Luo, and G. Z. Cheng, “Hydrolytic dehydrogenation of ammonia borane and methylamine borane catalyzed by graphene supported Ru@Ni core-shell nanoparticles,” *International Journal of Hydrogen Energy*, vol. 39, no. 1, pp. 426–435, 2014.
- [45] S. Akbayrak and S. Özkar, “Ruthenium(0) nanoparticles supported on multiwalled carbon nanotube as highly active catalyst for hydrogen generation from ammonia-borane,” *ACS Applied Materials & Interfaces*, vol. 4, no. 11, pp. 6302–6310, 2012.
- [46] Y. R. Fan, X. J. Li, X. C. He et al., “Effective hydrolysis of ammonia borane catalyzed by ruthenium nanoparticles immobilized on graphitic carbon nitride,” *International Journal of Hydrogen Energy*, vol. 39, no. 35, pp. 19982–19989, 2014.
- [47] M. Rakap, “Hydrogen generation from hydrolysis of ammonia borane in the presence of highly efficient poly(*N*-vinyl-2-pyrrolidone)-protected platinum-ruthenium nanoparticles,” *Appl Catal A-Gen.*, vol. 478, pp. 15–20, 2014.
- [48] S. Akbayrak, S. Tanyıldızı, İ. Morkan, and S. Özkar, “Ruthenium(0) nanoparticles supported on nanotitania as highly active and reusable catalyst in hydrogen generation from the hydrolysis of ammonia borane,” *International Journal of Hydrogen Energy*, vol. 39, no. 18, pp. 9628–9637, 2014.
- [49] Q. L. Yao, W. M. Shi, G. Feng et al., “Ultrafine Ru nanoparticles embedded in SiO₂ nanospheres: highly efficient catalysts for hydrolytic dehydrogenation of ammonia borane,” *Journal of Power Sources*, vol. 257, pp. 293–299, 2014.
- [50] N. Cao, T. Liu, J. Su, X. J. Wu, W. Luo, and G. Z. Cheng, “Ruthenium supported on MIL-101 as an efficient catalyst for hydrogen generation from hydrolysis of amine boranes,” *New Journal of Chemistry*, vol. 38, no. 9, pp. 4032–4035, 2014.
- [51] S. Akbayrak, M. Kaya, M. Volkan, and S. Özkar, “Ruthenium(0) nanoparticles supported on magnetic silica coated cobalt ferrite: reusable catalyst in hydrogen generation from the hydrolysis of ammonia-borane,” *Journal of Molecular Catalysis A: Chemical*, vol. 394, pp. 253–261, 2014.
- [52] N. Cao, K. Hu, W. Luo, and G. Z. Cheng, “RuCu nanoparticles supported on graphene: a highly efficient catalyst for hydrolysis of ammonia borane,” *Journal of Alloys and Compounds*, vol. 590, pp. 241–246, 2014.
- [53] S. Akbayrak and S. Özkar, “Ruthenium(0) nanoparticles supported on xonotlite nanowire: a long-lived catalyst for hydrolytic dehydrogenation of ammonia-borane,” *Dalton Transactions*, vol. 43, no. 4, pp. 1797–1805, 2014.
- [54] J. M. Yan, X. B. Zhang, H. Shioyama, and Q. Xu, “Room temperature hydrolytic dehydrogenation of ammonia borane catalyzed by Co nanoparticles,” *Journal of Power Sources*, vol. 195, no. 4, pp. 1091–1094, 2010.
- [55] K. S. Eom, K. W. Cho, and H. S. Kwon, “Hydrogen generation from hydrolysis of NH₃BH₃ by an electroplated Co-P catalyst,” *International Journal of Hydrogen Energy*, vol. 35, no. 1, pp. 181–186, 2010.